Supplementary information for Gravitational collapse of colloidal gels: Non-equilibrium phase separation driven by osmotic pressure

Poornima Padmanabhan and Roseanna N. Zia

Contents

1 Additional details on Methods

1.1 Description of wall potential

The gel is replicated periodically in the x and y directions of an orthogonal reference frame, whilst no-flux boundaries are imposed at the bottom ($z = 0$) and top ($z = H$) of the simulation cell to model a hard, flat, and impermeable floor and ceiling. The floor and ceiling were both modeled as a smooth and flat wall; their interaction with particles depends only on the distance of the center of the particle from the wall. Particles are prevented from passing through the wall via a steep repulsive potential. When particles approach the wall within 0.1 of their radius, the same physical attraction has twice the magnitude as the interparticle attraction because the wall does not diffuse.[1] LAMMPS[2] molecular dynamics package simulates a no-flux wall with an attractive potential via a Lennard-Jones potential, $V_{i,w}$:

$$V_{i,w}(r_w) = \begin{cases} 4\varepsilon\left[\left(\frac{\sigma}{r_{i,w}}\right)^{12} - \left(\frac{\sigma}{r_{i,w}}\right)^{6}\right], & r_{i,w} \le r_{cut,w} \\ 0, & r > r_{cut,w}. \end{cases} \quad (1)$$

Here, $r_{i,w}$ is the distance of the particle center from the wall. The parameters σ, ε, and $r_{cut,w}$ are tuned to recover the magnitude and length scale of the Morse potential between

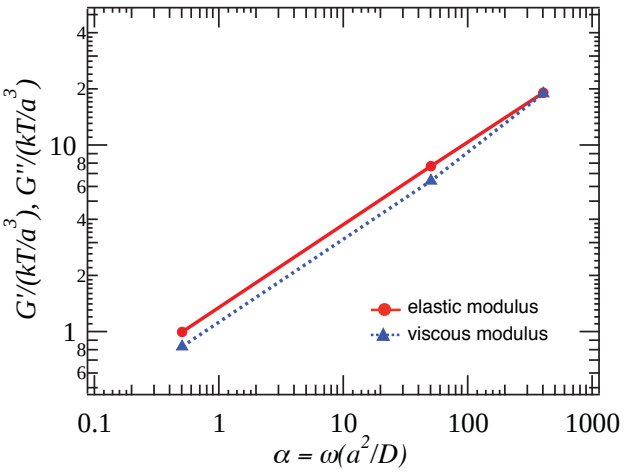

Figure S1: Elastic (G') and viscous (G'') moduli of a gel formed with $V_0 = 5kT$ aged in the presence of walls prior to onset of gravity.

a particle and a wall, leading to $r_{cut,w} = 0.32a$, $\sigma = 0.11a$, and

$$\varepsilon = \frac{2V_0}{1+4\left[\left(\frac{\sigma}{r_{cut,w}}\right)\right)^{12} - \left(\frac{\sigma}{r_{cut,w}}\right)^{6}\right]}. \tag{2}$$

1.2 Viscous and elastic moduli of initial gel

Linear-response moduli, G' and G'', are interrogated for the sample prior to gravitational loading to model the rheological properties of the gel. Following aging of the gel in the presence of the wall up to $500a^2/D$, a small-amplitude oscillatory shear is imposed $\dot{\gamma}(t) = \dot{\gamma}_0 \cos(\omega t)$, where $\dot{\gamma}_0$ is the amplitude of oscillation, ω is the frequency, and t is the time during the oscillatory cycle. The particle-phase stress was monitored throughout the oscillatory cycle and the elastic module G' and viscous modulus G'' were computed for a frequency sweep $0.4 \leq \alpha \leq 400$. The moduli were normalized on kT/a^3, and plotted against the frequency, made dimensionless on the Brownian time, $\alpha \equiv \omega a^2/D$ in Figure S1. The resulting moduli reveal that the elastic modulus dominates over viscous moduli over all examined frequencies, providing evidence that the gel is initially an elastic network.

2 Variation of volume fraction and gel morphology with Pe and V_0/kT

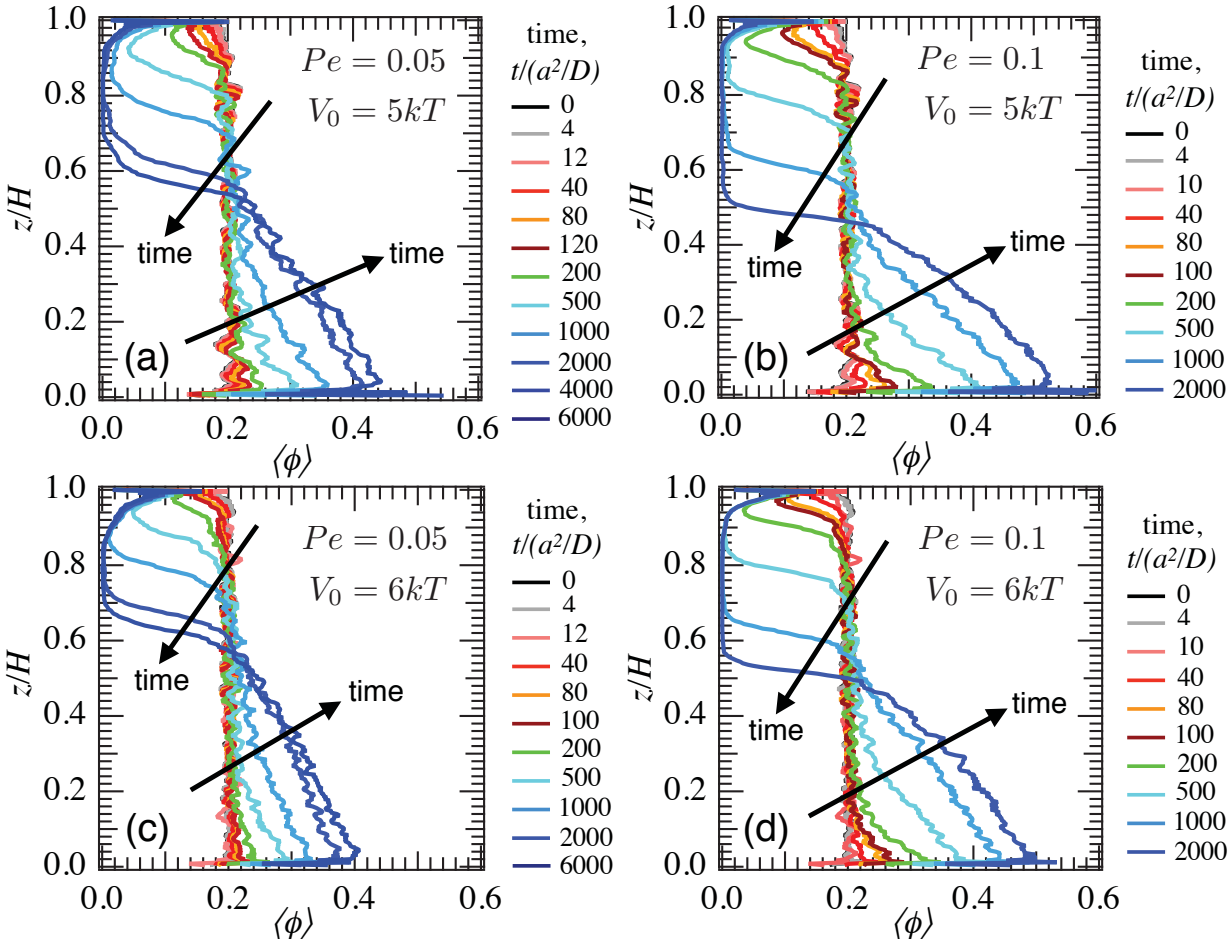

Figure S2: Layer-by-layer evolution of volume fraction in horizontal slices in the simulation cell, at several instants in time spanning the duration of collapse. Increasing gravitational forcing or particle weight, Pe, going from left to right, and increasing attraction strength, V_0/kT, from top to bottom.

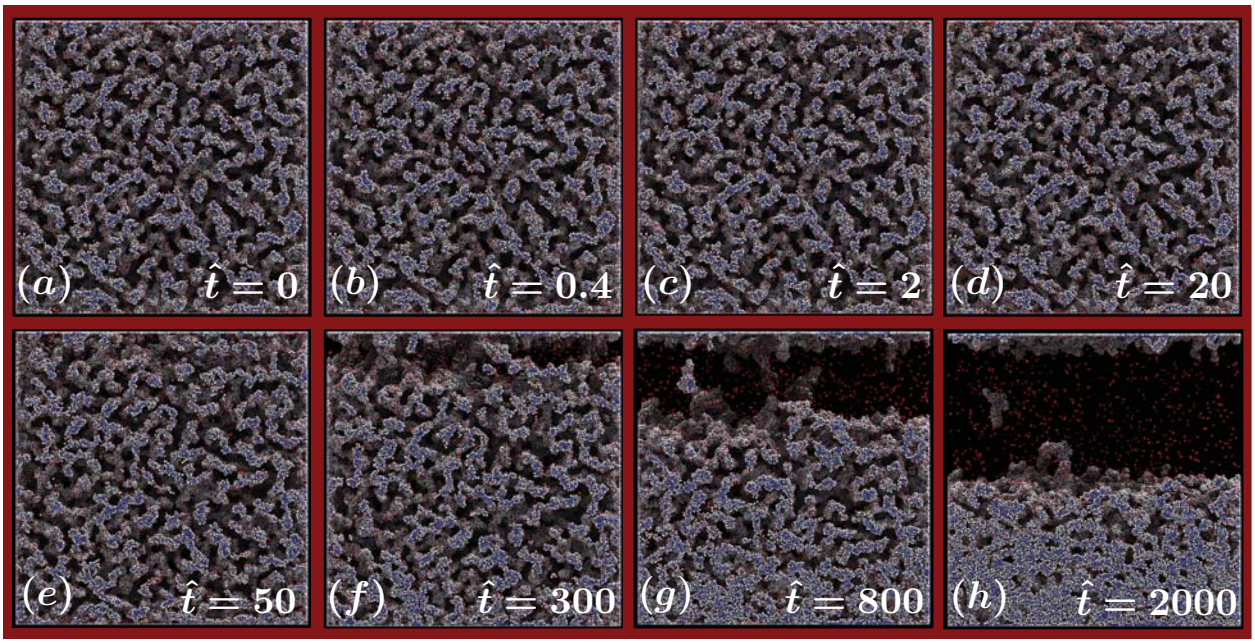

Figure S3: Snapshots of the gel with bond strength $V_0 = 5kT$ and particle weight $Pe = 0.1$ at several instants during sedimentation. Particles are colored according to the number of nearest-neighbor bonds, from red for zero or few bonds, to blue for many bonds.

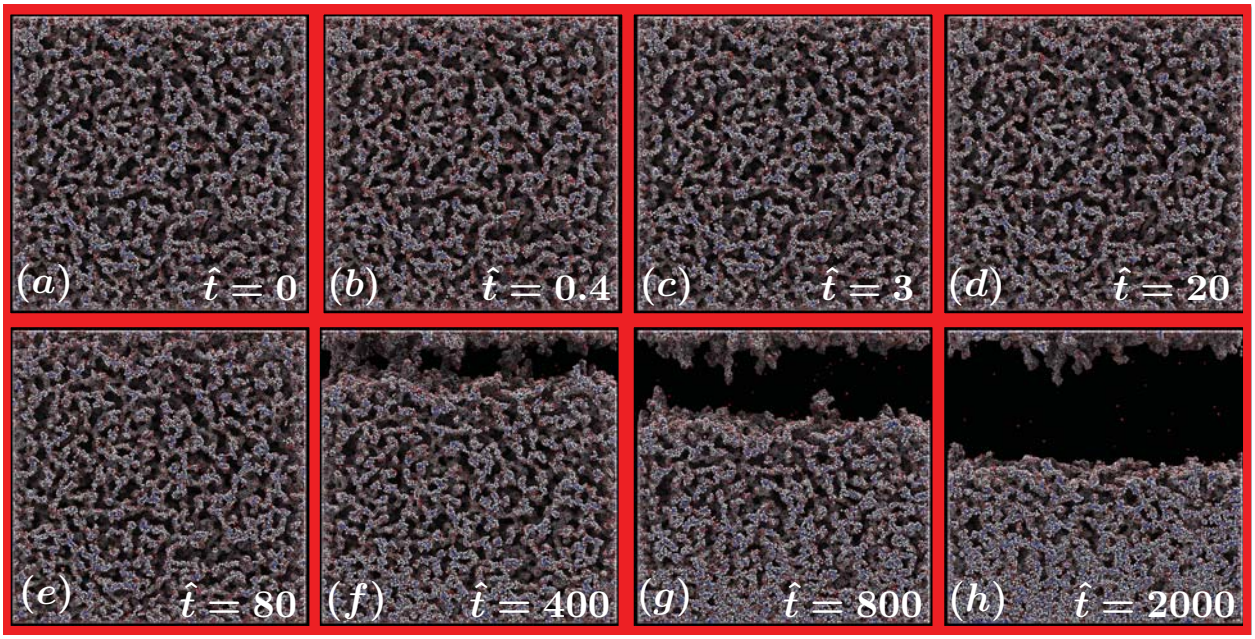

Figure S4: Snapshots of the gel with bond strength $V_0 = 6kT$ and particle weight $Pe = 0.1$ at several instants during sedimentation. Particles are colored according to the number of nearest-neighbor bonds, from red for zero or few bonds, to blue for many bonds.

3 Scaling of fall speed

Quantitative analysis of initial fall speed U_0 and peak fall speed U_{max} as they vary with bond strength reveals that increasing the strength of interparticle bonds actually amplifies the

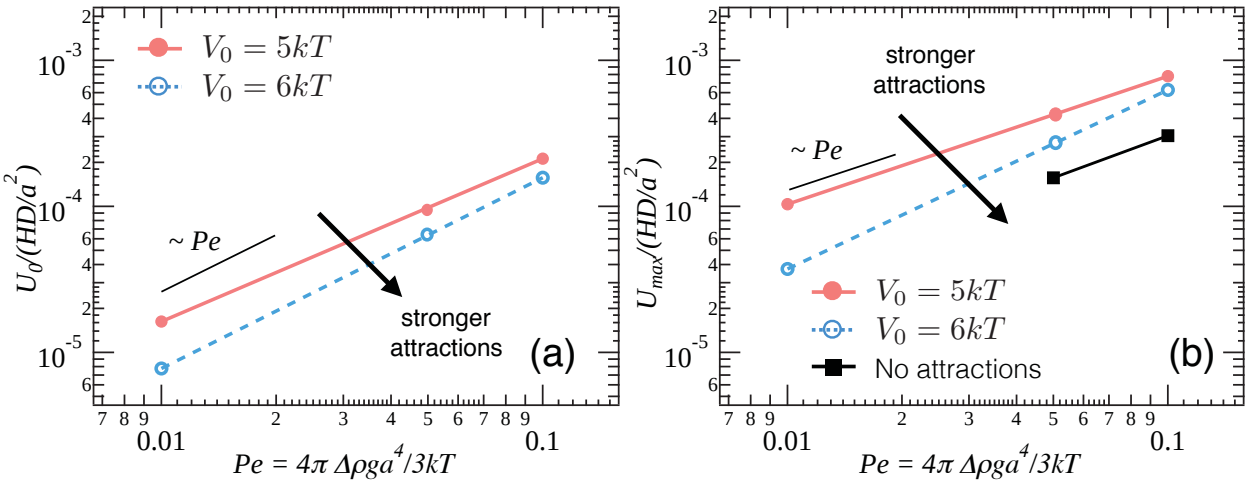

Figure S5: (a) Initial sedimentation rate, and (b) peak sedimentation rate, plotted as a function of particle weight, Pe.

fast-collapse sedimentation rate. Both U_0 and U_{max} are normalized on the diffusive speed of a particle alone in the solvent, and are plotted as a function of particle weight Pe, for two bond strengths, V_0/kT, in Figures S5a and S5b respectively. The initial sedimentation rate scales approximately linearly in Pe during induction, $U_0 \sim Pe^m$ with m slightly smaller than unity for weaker bonds. Surprisingly, the peak sedimentation rate (Figure S5b) shows that $U_{max} \sim Pe^m$ with $m \geq 1$, where stronger bonds give a larger value of m. That is, as V_0/kT weakens, $m \to 1$ as expected for a sedimenting suspension. When bonds are stronger, the gel falls faster. This result is counter-intuitive if one expects stronger bonds to produce a stronger gel network, i.e., that stronger bonds give a higher yield stress.

4 Additional data for collapsing gel for $Pe = 0.05$ and $V_0 = 5kT$

4.1 Zoomed-in snapshots near the ceiling

To connect pore growth adjacent to the ceiling, ,microstructural snapshots of the top 20% of the container are shown in Figure S6, where the vertical location of the pores adjacent to the ceiling are outlined in white. To track descent of the bulk of the gel, we select some solvent pores in the bulk, trace their outlines and track their temporal evolution. The same pores are monitored at $\hat{t} = 12$ in yellow, at $\hat{t} = 40$ in green, and at $\hat{t} = 120$ in cyan. Particles are colored according to the number of nearest-neighbor bonds, ranging from red for zero bonds (free diffusers) to white for several bonds, to blue for 10-12 bonds. Pore outlines reveal that beyond the tipping point, pores beneath the surface grow laterally and vertically, indicating that gravity enhances coarsening not only near the surface, but also in the bulk of the gel. Eventually, pore growth dissolves some strands (red arrow in Figure S6c) as particles migrate to lower-energy regions. As a strand narrows and slowly dissolves, it exposes new surface particles and free diffusers. The newly exposed high-energy surface smooths itself as particles seek to increase their contact number, i.e. coarsening continues.

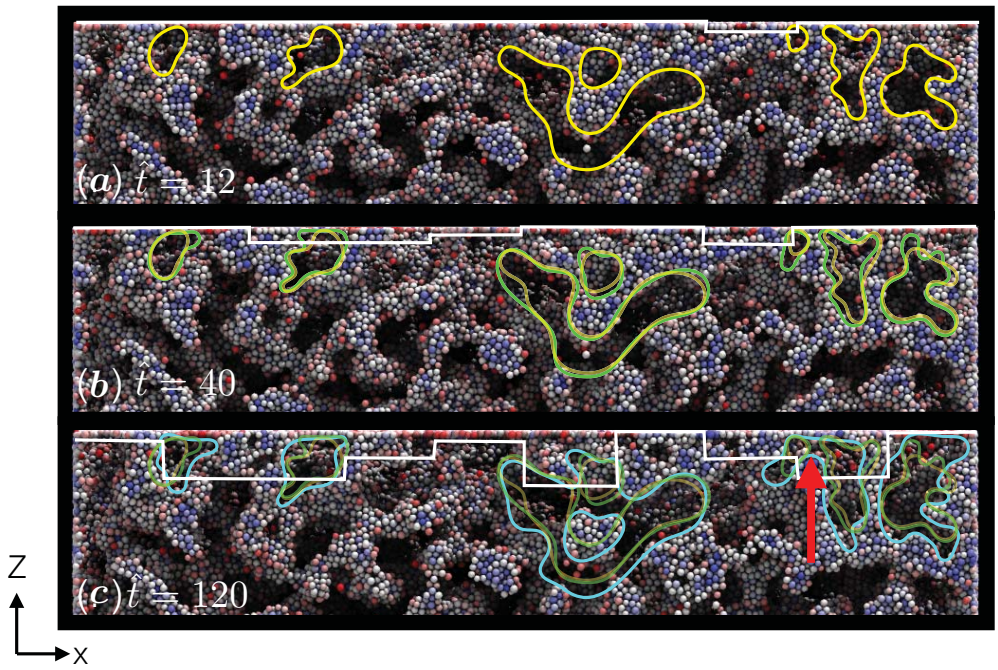

Figure S6: Zoomed-in view of the top 20% of the container showing the evolution of pores via particle migration. Particles are colored according to the number of nearest-neighbor bonds, from red for zero or few bonds, to blue for many bonds. White curve corresponds to the location of the rough, developing interface. Colored outline corresponds to selected pore shapes, colorized as (a) yellow at $\hat{t} = 12$, (b) green for $\hat{t} = 40$, and (c) cyan for $\hat{t} = 120$. For $V_0 = 5kT$, $Pe = 0.05$.

4.2 Volume fraction evolution

To quantify induction pore growth and other morphological changes presented qualitatively in Section 4.2, we zoom in to the volume fraction in the top 10% of the container, the top 10% of the gel, and the bottom 10% of the gel, in Figure S7, where each row corresponds to a temporal regime (induction, transition, fast sedimentation, and slow long-time compaction). A comparison between the left and middle columns gives a clear indication of whether the gel has begun to detach from the ceiling — if the curves are identical, the gel is still completely attached to the ceiling; if the curves differ, it signals ongoing or complete detachment. Volume-fraction, $\langle\phi\rangle(z)$, in the top 10% of the container and the gel are shown in plots (a) and (b) respectively, where each curve is a snapshot in time between $\hat{t} = 0$ and $\hat{t} = 12$. The curves are indistinguishable, confirming lateral pore growth but no vertical migration of particles away from the ceiling. Instead, the average volume fraction within the layers adjacent to the ceiling, and near the bottom (Figure S7c), remain unchanged during the induction period.

The transition point and fast collapse can now be analyzed quantitatively. The volume fraction plots in Figures S7d-e zoom in to the top 10% of the container and the gel during this transition period. The curves corresponding to the same instant in time differ between (d) and (e) near the top 2% corresponding to the small macroscopic deformation; therefore, the gel has begun to detach from the ceiling. At the peak sedimentation rate, $\hat{t} = 120$, Figure S7f reveals densification at the bottom of the container, significantly larger than the quiescent fluctuations associated with bi-continuous morphology, $\langle\phi\rangle(z) \simeq 25\%$.

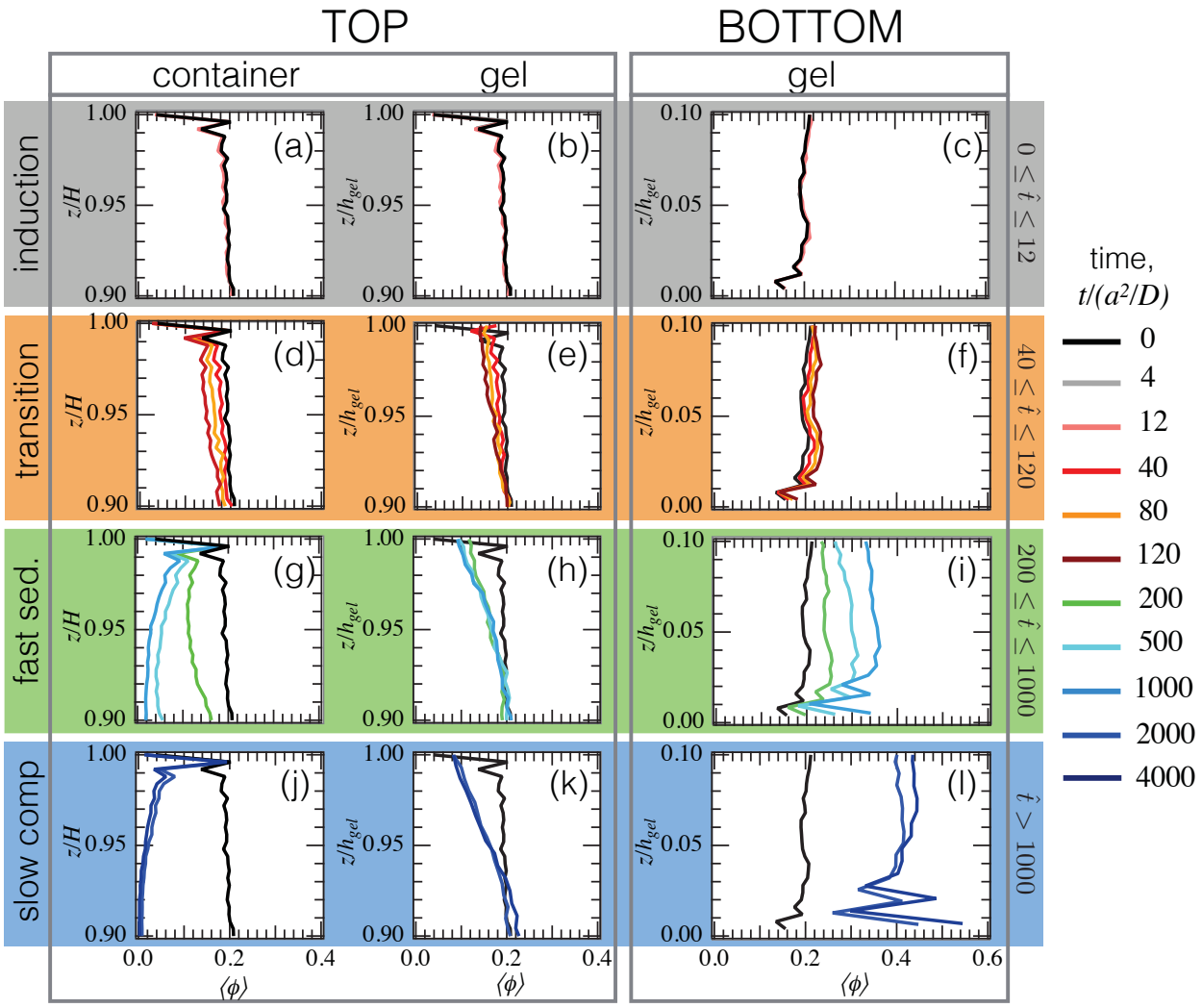

Figure S7: Zoomed-in layer-by-layer evolution of volume fraction in horizontal layers for a gel $V_0 = 5kT$, forced at $Pe = 0.05$ over four temporal regimes of collapse.

Overall, distinct spatial zones emerge during the transition regime but the decrease in volume fraction near the ceiling does not correspond to the emergence of a container-wide supernatant; only a partial, free rough surface. This further suggests that the capillary-like instability grows beyond the tipping point, as strands dissolve toward network junctions, leading to eventual ceiling detachment.

The volume fraction during rapid sedimentation, $120 \leq \hat{t} \leq 1200$, is plotted in Figures S7g-i (highlighted in green). Here, strands dissolve, causing pores to coalesce, colloid-poor regions begin to form and grow near the top of the container. Correspondingly, volume fraction continues to decrease in Figure S7g but is not zero, providing macroscopic evidence that detachment of the gel from the ceiling is still ongoing. In this regime, curves in the left and middle columns significantly differ as the gel descends away from the ceiling, and the top of the gel moves outside the view of the left column. Here, the middle column reveals information about the roughness of the interface separating the gel and the region above it; the top 10% of the gel has a significant portion with volume fraction below 20% (Figure S7h), suggesting that the roughness of the interface is several particles thick. Over time, the volume fraction curves become progressively flatter, as the interface that bridges the gel and the supernatant becomes sharper and the exposed gel surface smoothens.

Quantitative measurements of volume fraction support the visual observation of a container-wide supernatant in Figure S7j where $\langle\phi\rangle \rightarrow 0$ at $\hat{t} > 1000$. The interfacial region (Figure S7k) thins over time, with the $\langle\phi\rangle \simeq 20\%$ region creeping slowly upward toward $z/h_{gel} \simeq 94\%$, and the topmost layer at $\langle\phi\rangle \simeq 10\%$ and slowly depleting. The middle zone has disappeared. By this time, the sedimentation rate decays rapidly and collapse ceases, indicating that when the gel can densify no further, collapse stops.

4.3 Contact number distribution over the entire gel

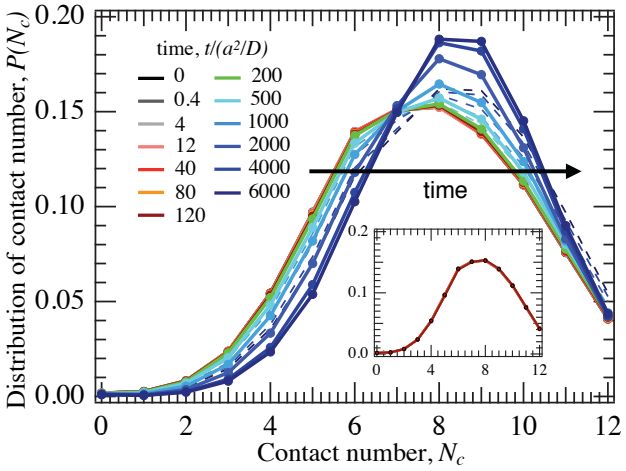

Figure S8: Evolution of contact number distribution with time for a $5kT$ gel with particle weight $Pe = 0.05$ (solid lines) and undergoing quiescent coarsening (dashed lines).

To connect densification to contact number evolution, the contact number distribution, $P(N_c)$, is plotted for the entire gel over the duration of collapse in Figure S8. To compare with quiescent coarsening, two sets of data are shown for several instants in time, one with particle weight $Pe = 0.05$ (solid lines), alongside a gel coarsening under quiescent

conditions, in the presence of container boundaries (dashed lines). For the two sets of data, the gels have identical morphologies at $\hat{t} = 0$.

Initially, the most common contact number is $N_c = 8$, but the distribution of contact number for the quiescent aging gel shifts to the right slightly over time, as particles migrate to regions of higher contact number that reduce potential energy, in what has been argued to be ongoing slow phase separation.[3] A markedly more rapid shift takes place in the collapsing gel (solid curves), with decreasing potential energy, suggesting more rapid phase separation. Even at long times, $\hat{t} \geq 2000$, with little to no macroscopic change in bulk height or average volume fraction, an increase in the peak of $P(N_c)$ suggests ongoing restructuring of the gel.

The inset zooms in on the early-time behavior ($0 \leq \hat{t} \leq 120$), for quiescent ($Pe = 0$) and loaded ($Pe = 0.05$) gels. Even though we saw growth in pore size, early-time changes in $P(N_c)$ appear to be difficult to distinguish, in agreement with $\langle N_c \rangle(t)$, because the mobile particles that drive coarsening belong to the population $N_c \in [0,3]$, which constitute fewer than 4% of all particles in the gel. A small change in population of these particles is difficult to detect from $P(N_c)$ curves, but one can tease out the changes relative to the initial population size by normalizing the distribution at any time $\hat{t}$ by its value at $\hat{t} = 0$, examined in the main text.

4.4 Comparison of middle layer evolution to attractive glass

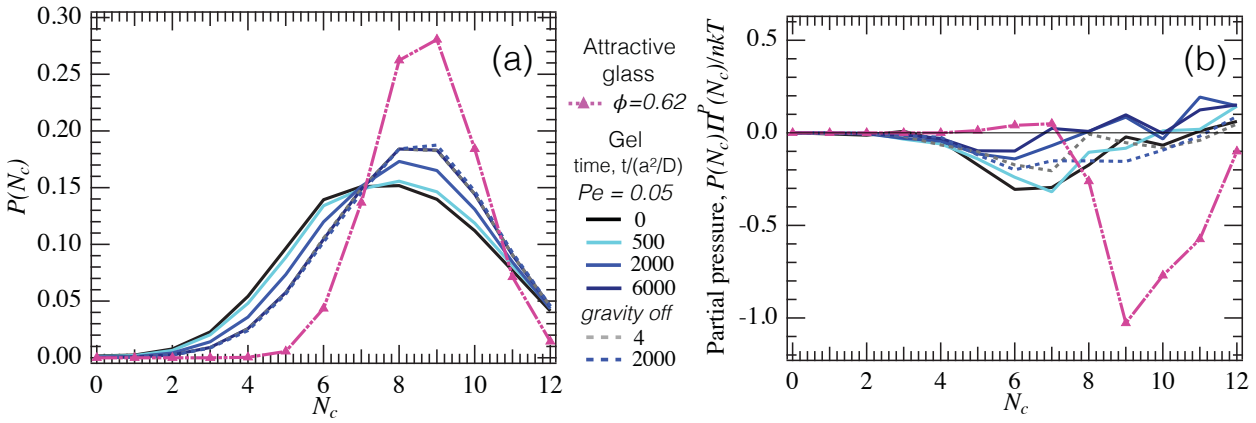

Figure S9: Comparison of the attractive glass and the bottom layer of the gel ($0.1 \leq z/h_{gel} \leq 0.2$) with bond strength $V_0 = 5kT$ during collapse and after shutting off gravity. (a) Contact-number distribution, $P(N_c)$, and (b) partial pressure, normalized on nkT.

We compare the collapsing gel to an attractive glass prepared from a repulsive glass of volume fraction $\phi = 0.62$, where an attractive interparticle potential is imposed, as would occur by adding depletant to a repulsive glass in an experiment.[4] We compare the contact number distribution in the bottom layer in the gel to that of the attractive glass in Figure S9a. The two most important features of the data for the attractive glass are a sharp peak at $N_c = 9$, and a vanishingly small population for $N_c \leq 4$ that, combined, confirm that it is devoid of pores of more than a particle size, and is devoid of surface particles. In contrast, the bi-continuous gel initially exhibits a broad distribution where extensive surface area permits a significant population size for $N_c \leq 4$. During collapse ($0 \leq t \leq 6000$), the distribution in the gel moves toward the right and is more sharply peaked as pores shrink, and moves toward the distribution of the attractive glass, but

never completely so, evidently prevented by re-arrest due to gravity. Remarkably, after gravitational forcing is removed, Figure S9a reveals that a small change in contact number distribution (in contrast to the barely discernible change in the bottom layer) after 2000 Brownian times, suggesting that further condensation is very slow, despite the negative osmotic pressure. This suggests that glassy frustration is too deep (particle mobility is low).

That is, it appears that the requirement for condensation is not only a negative osmotic pressure, but also that the particles with negative osmotic pressure are mobile enough to drive bond relaxation.

A better predictor of collapse is the partial pressure exerted by each population that can reveal whether mobile, surface particles contribute to the negative osmotic pressure, in which case jamming will prevent phase separation. The partial pressure of each N_c population (the per-particle pressure weighted by its population size), is normalized on nkT and plotted as a function of N_c in Figure S9b. The primary features of the partial pressure in the attractive glass are a zero pressure for $N_c \leq 4$, and sharply negative values for $N_c \geq 7$. The single-phase domain with no surface area (the attractive glass) drives the former effect. The latter effect evidences deep glassy frustration, where bonds are pulled out of their wells and held stretched by jammed morphology. In contrast, in the gel, the partial pressure for the middle layer is *initially* negative for $N_c \leq 10$ with a negative minimum at $N_c = 6$; that is, sufficiently mobile populations have a negative osmotic pressure.

During the first three regimes of collapse ($0 \leq \hat{t} \leq 1400$) collapse, it is the negative partial pressure of mobile particles in the middle layer that drives condensation, and densification of the gel. Eventually, affine compaction pushes particles toward one another, and the partial pressure becomes positive for $N_c \geq 7$ by $\hat{t} = 6000$. By shutting off gravity, these compressed bonds relax and partial pressure becomes once again negative for all populations. However, the partial pressure now exhibits a negative peak at $N_c = 9$ after removal of gravity, differing from the initial gel, and revealing similarities to the attractive glass for $N_c \geq 9$, suggesting re-arrest of the gel.

4.5 Bond-length distribution

During collapse, the potential energy of the gel decreases suggesting that the bonds in the gel relax toward the minimum, and eventually, osmotic pressure increases as bonds undergo compression. Further evidence of bond relaxation and subsequent bond compression are obtained by examining the bond-length distribution per particle. The number of bonds per particle at bond length s, $N(s)$ is computed, and the growth is tracked by taking the difference between $N(s)$ and its initial value are plotted in Figure S10 for several instants in time for the middle and bottom layers. The red shaded region mark compressed bonds while the yellow shaded region marks stretched bonds.

The middle layer reveals minor fluctuations in bond distribution during the induction period $0 \leq \hat{t} \leq 12$. During the transition regime and into fast sedimentation, N_c increases, and the resulting bond-length distribution increases near the minimum $s = 0$, as several bonds relax during collapse. Eventually, $\hat{t} \geq 1000$, when densification occurs and causes affine compaction, the peak shifts to the left of $s = 0$ indicating that many compressed bonds grow, resulting in an overall positive osmotic pressure. This bond compression, although small, relaxes after gravity is turned off, allowing phase separation to progress.

The bottom layer is always undergoing affine displacements and the shift in bonds toward compressed lengths is more evident by an increase in overall magnitude over the

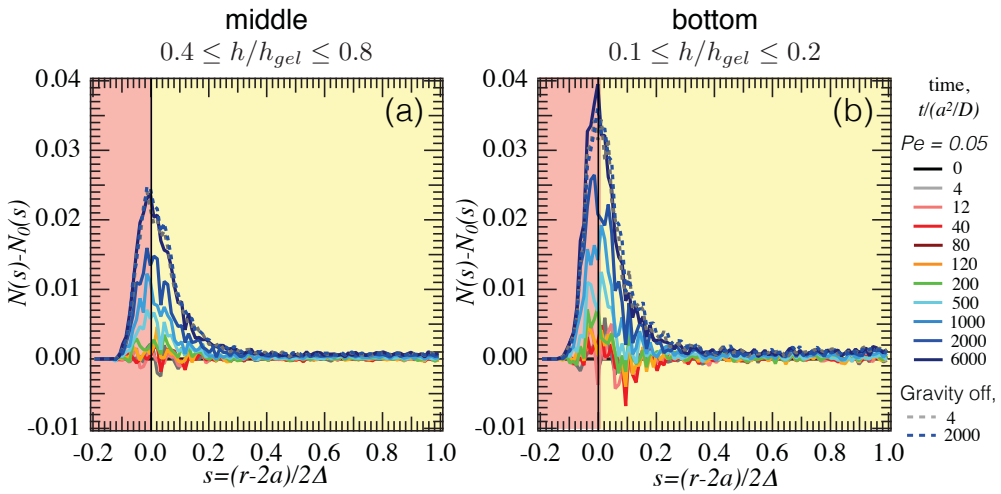

Figure S10: Difference in bond-distance distribution for several instants in time with and without gravity for (a) middle layer in the gel ($0.4 \le z/h_{gel} \le 0.8$) and (b) bottom layer in the gel ($0.1 \le z/h_{gel} \le 0.2$). For $V_0 = 5kT$ and $Pe = 0.05$.

duration of collapse. During the induction period, no detectable growth in bonds occurs. Subsequently, during the transition regime, bonds grow at all lengths, but the growth in bonds at $s < 0$ is even more pronounced, suggesting that affine compaction results in bond compression, creating more compressed bonds and depleting stretched bonds. Eventually bonds of all lengths grow, resulting in the peak occurring at $s < 0$ and thereby, a positive osmotic pressure that suppresses phase separation. Finally, When gravity is turned off, the peak shifts toward the right, suggesting that compressed bonds relax, and a strongly negative osmotic pressure can arise from the stretched bonds.

5 Osmotic pressure for a short-ranged interparticle potential

The effect of particles and their interactions on osmotic pressure has been defined mechanically as the particle contributions to the negative of the trace of the equilibrium stress tensor,[5–7]

$$\frac{\Pi}{nkT} = -\frac{1}{3}\frac{\boldsymbol{I} : \langle \boldsymbol{\Sigma} \rangle}{nkT} = 1 + \frac{\Pi^P}{nkT} + \ldots, \tag{3}$$

where the first term on the right hand side is the ideal osmotic pressure and is always positive: diffusion tends to expand system boundaries.[6] The pair contribution Π^P can raise or lower osmotic pressure. A positive pair contribution to osmotic pressure also tends to expand a system outward, while condensing systems display $\Pi^P < 0$.[3,6] Only the elastic stress $n\langle \boldsymbol{x}\boldsymbol{F}^P \rangle$ matters in a freely draining system, where hard-sphere repulsion (entropic exclusion) gives a positive osmotic pressure, and attractions give a negative contribution:

$$\frac{\Pi^P}{nkT} = \frac{\langle \boldsymbol{r} \cdot \boldsymbol{F} \rangle}{3kT}, \tag{4}$$

where $\boldsymbol{r} \equiv \boldsymbol{X}_i - \boldsymbol{X}_j$ is the separation between a pair of particles i and j at positions $\boldsymbol{X}_i$ and $\boldsymbol{X}_j$ respectively, and $\boldsymbol{F}$ is the force derivable from the interparticle potential (cf Equation **??**) for that separation. The angle brackets denote a sum over all pairs of interactions, divided by the number of particles.

If a gas is sufficiently dilute it is assumed to be ideal, meaning that the only contributions to pressure arise from the finite size and energy of individual particles. Pair interactions are negligible, so effects such as attractions that would reduce kinetic energy, and therefore pressure, can be neglected. If such a gas is multicomponent such that different species have different kinetic energies we can simply sum their contributions as individuals. The $O(n^2)$ in Equation 3 term in the virial expansion is irrelevant. Dilute colloidal dispersions can be analyzed analogously.

But in a dense suspension, three or more particles can encounter one another simultaneously. Long-range interactions can produce hierarchical N-body couplings, contributing to higher order terms in the virial expansion that may not be simply neglected. However, if particle interactions are short-ranged, it is possible to approximate the interactions between several particles in a cluster as pairwise. In the case of attractions arising from a depletion force, it must be determined whether the osmotic pressure gradient of depletant for the formation of a new bond is weaker or stronger due to the presence of a prior bond. The maximum attraction strength for a pairwise depletion interaction is given by:[8,9]

$$\frac{V_{dep}}{kT} = n_b^{\infty} V_{overlap} = n_b^{\infty} \frac{2}{3} \pi a^3 \Delta^2 (3 + 2\Delta), \tag{5}$$

where V_{dep} is the interaction potential, $V_{overlap}$ is the excluded volume due to the overlap of the interacting particles, n_b^{∞} is the bulk depletant number density, a is size of the colloid, and Δ is the ratio of sizes of the depletant to colloid. We examine the formation of subsequent bonds as the cluster grows. For a given depletant to colloid size ratio, the maximum attraction strength linearly depends on the volume of overlap and the bulk depletant concentration. Therefore, in order to determine whether formation of one bond affects the interaction strength of subsequently formed bonds, we will examine these separately starting with the overlap volume.

In order to calculate the total overlap volume for a cluster of particles, one must calculate the total volume excluded to the depletant in the intervening gaps between the particles in the cluster. The total volume excluded in the cluster is given by the sum of pairwise excluded volumes accounting for any overlap between overlaps (shared excluded volumes), which we call overlap between overlaps. This over counting depends on the steric hindrance due to the other colloids in the cluster. But due to hard sphere exclusion, the volumes excluded to the depletants from each pair interaction within the cluster cannot overlap if it results in the overlap of colloids. That is, steric hindrance from the colloids prevents some over counting. If steric hindrance can prevent *all* over counting, then the total volume excluded to the depleting in the intervening gaps is simply the sum of pairwise excluded volumes. We determine possibility of such a scenario.

The geometric constraint such that over counting is sterically-hindered is when $\Delta \leq \Delta_{crit} = \frac{2}{\sqrt{3}} - 1 \simeq 0.15$.[10,11] Therefore, for the interaction potential used in our simulation where $\Delta = 0.1$, the colloids sufficiently hinder each other such that the overlap volume in the cluster is the sum of overlap volumes of each pair in the cluster (see Figure S11 for an illustration). When $\Delta = 0.1$ (Figure S11a), there is no overcounted volume and therefore the total overlap volume is exactly the sum of pairwise overlaps. When $\Delta = 0.2$ (Figure S11b)and larger than the critical value, some volume is overcounted when the particles are at their closest approach. However, when the average coordination number is high, bonds are often held out of their minima due to glassy frustration and neglecting

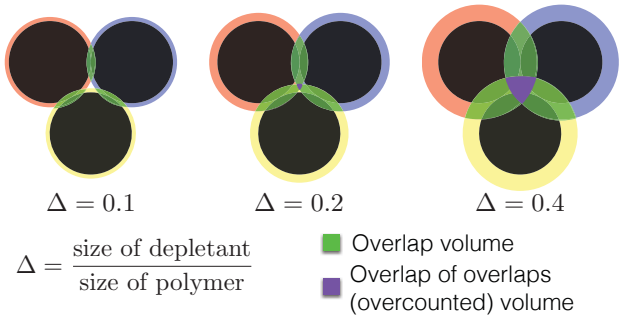

Figure S11: Excluded volume in green for various ratios of depletant-colloid sizes. Black circles indicate the excluded volume of the hard particles, colored annuli represent the range of the depletion attraction interaction. Regions shaded in green correspond to the overlap volume when two colloids are at the closest approach, and the purple regions mark the overlap of regions shaded in green.

higher-body terms may be a valid approximation. When $\Delta = 0.4$ (Figure S11c), overcounted volume is significant and a pairwise approximation of the osmotic pressure is not expected to be valid.

For the colloidal gel examined in this study, the range of depletion attraction $\Delta = 0.1$, and the volume of overlap calculation is exactly the sum of all pairwise volume overlaps. Thus, when the bulk concentration of depletant (and chemical potential) is assumed constant, neglecting higher order terms in Equation 3 is valid.[10,11] We now turn our attention to the effective change in bulk concentration when the volume available to the depletant increases due to a decrease in intervening gaps that drives depletion attraction. The bulk density of depletant is given by:

$$n_b^{\infty} = \frac{\#\text{ depletants in container}}{V_{free}}, \tag{6}$$

where V_{free} is the free volume available to the depletant in the container. If there are no particle overlaps, the volume available to the depletant is given by:

$$V_{free} = V(1 - \phi(1+\Delta)^3), \tag{7}$$

where V is the volume of the container, ϕ is the volume fraction of colloids. If bonds are formed between many particles in the system, the available volume for the particles increase by the total overlap volume formed by all bonds. Thus, the new free volume available is V'_{free}. Since the total number of depletants in the container is fixed, the new depletant bulk density $n_b'^{\infty}$ decreases, given by

$$\frac{n_b'^{\infty}}{n_b^{\infty}} = \frac{V_{free}}{V'_{free}} \tag{8}$$

Calculation of an exact value of V'_{free} is not straightforward because it depends on the instantaneous configurations of particles. In the limit that all bonds that form occur at maximum overlap, we can obtain the additional free volume as the sum of free volume per bond times the number of bonds in the container. This value must further be divided by 2 to account for overcounting the bonds. The excess free volume, V^{excess} is given by:

$$V_{excess} = V_{overlap} \frac{\langle N_c \rangle \times \text{number of colloids}}{2} \tag{9}$$

$$V_{excess} = V_{overlap} \frac{\langle N_c \rangle}{2} \times \frac{\phi V}{\frac{4\pi}{3} a^3} \tag{10}$$

Finally, $V'_{free} = V_{free} + V^{excess}$.

$$\frac{n_b'^{\infty}}{n_b^{\infty}} = \frac{1}{1 + \frac{V_{excess}}{V_{free}}} \tag{11}$$

$$\frac{V_{excess}}{V_{free}} = \frac{\frac{2}{3}\pi a^3 \Delta^2 (3+2\Delta) \frac{\langle N_c \rangle}{2} \phi}{\frac{4\pi}{3} a^3 [1 - \phi(1+\Delta)^3]} = \frac{\Delta^2 (3+2\Delta) \langle N_c \rangle \phi}{4[1 - \phi(1+\Delta)^3]} \tag{12}$$

For typical values for the colloidal gel studied in this work, where $\phi = 0.2$, $\langle N_c \rangle = 8$, $\Delta = 0.1$, we get

$$\frac{n_b'^{\infty}}{n_b^{\infty}} = 0.983. \tag{13}$$

The change in number density of depletant is less than 2%, which implies that the change in the attraction potential due to particles on average forming clusters of 8 particles is less than 2%. In reality, the bond distances in a colloidal gel are on average held out of equilibrium, and the actual increase in volume available to the depletant will be even smaller, resulting in a smaller change in number density, and therefore even smaller change in the attraction potential. Thus, for a colloid-polymer system with $\Delta = 0.1$, the pairwise depletion attraction potential is a valid approximation even when many-body clusters form, and the resulting osmotic pressure is accurate to $O(n^2)$.

References

[1] H. N. W. Lekkerkerker and R. Tuinier, *Colloids and the depletion interaction*, Springer Netherlands, 2011.

[2] S. Plimpton, *J Comp Phys*, 1995, **117**, 1 – 19.

[3] R. N. Zia, B. J. Landrum and W. B. Russel, *Journal of Rheology*, 2014, **58**, 1121–1157.

[4] K. Pham, S. Egelhaaf, P. Pusey and W. Poon, *Physical Review E*, 2004, **69**, 011503.

[5] J. F. Brady, *J. Chem Phys.*, 1993, **98**, 3335–3341.

[6] R. N. Zia and J. F. Brady, *J. Rheol.*, 2012, **56**, 1175–1208.

[7] H. C. W. Chu and R. N. Zia, *Journal of Rheology*, 2016, **60**, 755 – 781.

[8] S. Asakura and F. Oosawa, *J. Chem. Phys.*, 1954, **22**, 1255–1256.

[9] A. Vrij, *Pure and Applied chemistry*, 1976, **48**, 471–483.

[10] A. P. Gast, C. K. Hall and W. B. Russel, *Journal of Colloid and Interface Science*, 1983, **96**, 251–267.

[11] M. Dijkstra, J. M. Brader and R. Evans, *Journal of Physics: Condensed Matter*, 1999, **11**, 10079–10106.